Selenic Acid Etching Assisted Atomic Engineering for Designing Metal-Semimetal Dual Single-atom Catalysts for Enhanced CO_2 Electroreduction

Minghong Huang,[†,§] *Shenghua Zhou,*[§] *Cheng-Jie Yang,*[‡] *Chung-Li Dong,*[‡] *Yingchun He,*[§] *Wenbo Wei,*[§] *Xiaofang Li,*[§] *Qi-Long Zhu,*[*,§,∥] *and Zhenguo Huang*[*,†]

[†] School of Civil and Environmental Engineering, University of Technology Sydney, Ultimo, New South Wales 2007, Australia

[§] State Key Laboratory of Structural Chemistry, Fujian Institute of Research on the Structure of Matter, Chinese Academy of Sciences (CAS), Fuzhou 350002, China

[‡] Department of Physics, Tamkang University, Tamsui 25137, Taiwan

[∥] School of Materials Science and Engineering, Zhejiang Sci-Tech University, Hangzhou 310018, China

KEYWORDS: electrocatalysis, CO_2 reduction, single-atom catalysts, atomic structure engineering, Zn-CO_2 battery

ABSTRACT: Single-atom catalysts are promising for electrocatalytic CO_2 conversion but face challenges in controllable syntheses. Herein, a facile selenic acid etching-assisted strategy has been

developed to fabricate a hybrid metal-semimetal dual single-atom catalyst for electrocatalytic CO_2 reduction. This strategy enables the simultaneous generation of monodisperse active sites and hierarchical morphologies with hollow nanostructures. The as-obtained catalyst with Fe-Se dual single-atom sites supported by porous nitrogen-doped carbon (FeSe-NC) shows exceptional catalytic activity and CO selectivity, delivering a Faradaic efficiency (FE) of >97% with industrially comparable j_{CO}, superior to the Fe single-atom catalyst. Moreover, the FeSe-NC-based rechargeable Zn-CO_2 battery delivers a high power density (2.01 mW cm^{-2}) and outstanding FE_{CO} (>90%), as well as excellent cycling stability. Experimental results together with theoretical calculations reveal that the etching-induced defects and the Se-modulated Fe centers with asymmetrical polarized charge distributions synergistically facilitate the key intermediate *CO desorption, and thus accelerate the CO_2-to-CO conversion.

Electrocatalytic CO_2 reduction reaction (CO_2RR), an effective CO_2 conversion technology, is promising for lowering anthropogenic CO_2 emissions while producing value-added carbonaceous fuels.[1, 2] However, such technologies usually require catalysts with high activity to selectively convert CO_2 to target products. Electrochemical reduction of CO_2 to CO via two-electron transfer is attractive since it produces an essential feedstock for chemical and industrial production.[3] Thus, there have been intensive efforts devoted to developing effective catalysts for electrocatalytic CO_2 reduction to CO, such as noble metal-based and molecular materials.[4, 5] However, their high costs and poor durability are roadblocks for commercial applications.

Beyond precious metal-based catalysts, one ideal alternative is atomically dispersed metal atom based catalysts, known as single-atom catalysts (SACs), which have demonstrated great potential in CO_2RR owing to their distinctive catalytic features.[6-11] Iron-based SACs with nitrogen doped carbon (NC) supports, noted as Fe-NC, for example, are highly active for selective CO production, which can be on par with or even superior to precious metal catalyst.[12-14] However, the performance associated with those reported Fe SACs still suffers from limited current density and easy poisoning at the Fe-N_4 sites by *CO intermediate at high potentials.[15, 16] To improve the performance of Fe SACs, an effective approach is the atomic engineering of the single metal atoms,[7, 8, 17] where regulating the coordination to construct dual-metal atomic catalysts (DACs) has been particularly attractive.[18-20] Building DACs, specially hybrid DACs, offers great potential since it effectively modifies the local atomic environment and creates extra metal sites.[21-25] Synergistic active sites with different but favorable adsorption energies, as a promoter, improve the reaction kinetics. Recently, Ren and co-workers introduced the concept of binary atomic engineering to construct isolated Ni-Fe DAC sites, which significantly improved CO_2-to-CO conversion.[25] Similarly, a series of DACs with or without axial heteroatom bridging supported by NC showed better activity and CO selectivity than monometallic catalysts.[22, 26] These reports demonstrate that heteroatom doping, geometric structures, electron distribution, and metal–metal interactions all affect the CO_2RR performance of these DACs. The induced electronic regulation can facilitate the reaction process by producing key intermediates and suppress competing hydrogen evolution reaction (HER). However, to fabricate DACs with suitable metal atoms is synthetically challenging. The common approaches reported so far for preparing DACs are co-crystallization, ion exchange, atomic replacement, and cage confinement.[27-30] Nevertheless, simultaneous generation of single-atom sites and controllable pore engineering have been rarely

reported. The bulky particles and narrow pores in most metal-organic frameworks (MOF)-derived DACs severely limit the mass transfer in the catalysts, resulting in sluggish CO_2RR kinetics. Therefore, developing effective methods to fabricate DACs with hierarchical porous structures and understanding their structure-activity relationship is of great scientific and technological importance.

By selectively breaking the coordination bonds between metal ions and organic linkers, chemical etching of MOFs provides an effective means to simultaneously tailor the shape and composition of the derivatives.[31, 32] Aqueous solutions of SeO_2, a weak acidic etching agent, can slowly etch the MOF precursors and also introduce selenium to form selenium-rich nanostructures.[33, 34] Selenium, a semi metal with chemical properties similar to sulfur but higher polarizability, is expected to have catalytic activity for CO_2RR.[35, 36] Therefore, we envision that coupling *p*-block Se single atom (SA) with *d*-block Fe SA may enhance CO_2RR performance due to a synergistic catalytic effect. So far, metal-semimetal DACs have rarely been reported, and the correlation between their structures and CO_2RR performance requires investigations.

Herein, we report a selenic acid etching assisted strategy to obtain isolated metal-semimetal dual atomic sites. By treating the SeO_2-etched zeolitic imidazolate frameworks (ZIF) precursor, Se can be *in situ* doped into the porous N-doped hierarchical hollow carbon matrix and subsequently combined with Fe SAs to form Fe-Se DACs. Benefiting from Se-induced electronic structure change for the Fe centers, the resultant FeSe-NC delivered a high CO selectivity of up to 97% in a H-type cell and affords an industrially comparable j_{CO} (>228 mA cm^{-2}) in a flow cell. Furthermore, a rechargeable Zn-CO_2 battery (ZCB) using the as-synthesized FeSe-NC as the cathode delivered a high power density (2.01 mW cm^{-2}) and superior FE_{CO} (>90%), offering great potential for practical applications. This study presents an effective approach for optimizing the

electronic structures of atomic catalysts and the adsorption/desorption dynamics of intermediates on active sites, thus enhancing their electrocatalytic performance.

RESULTS AND DISCUSSION

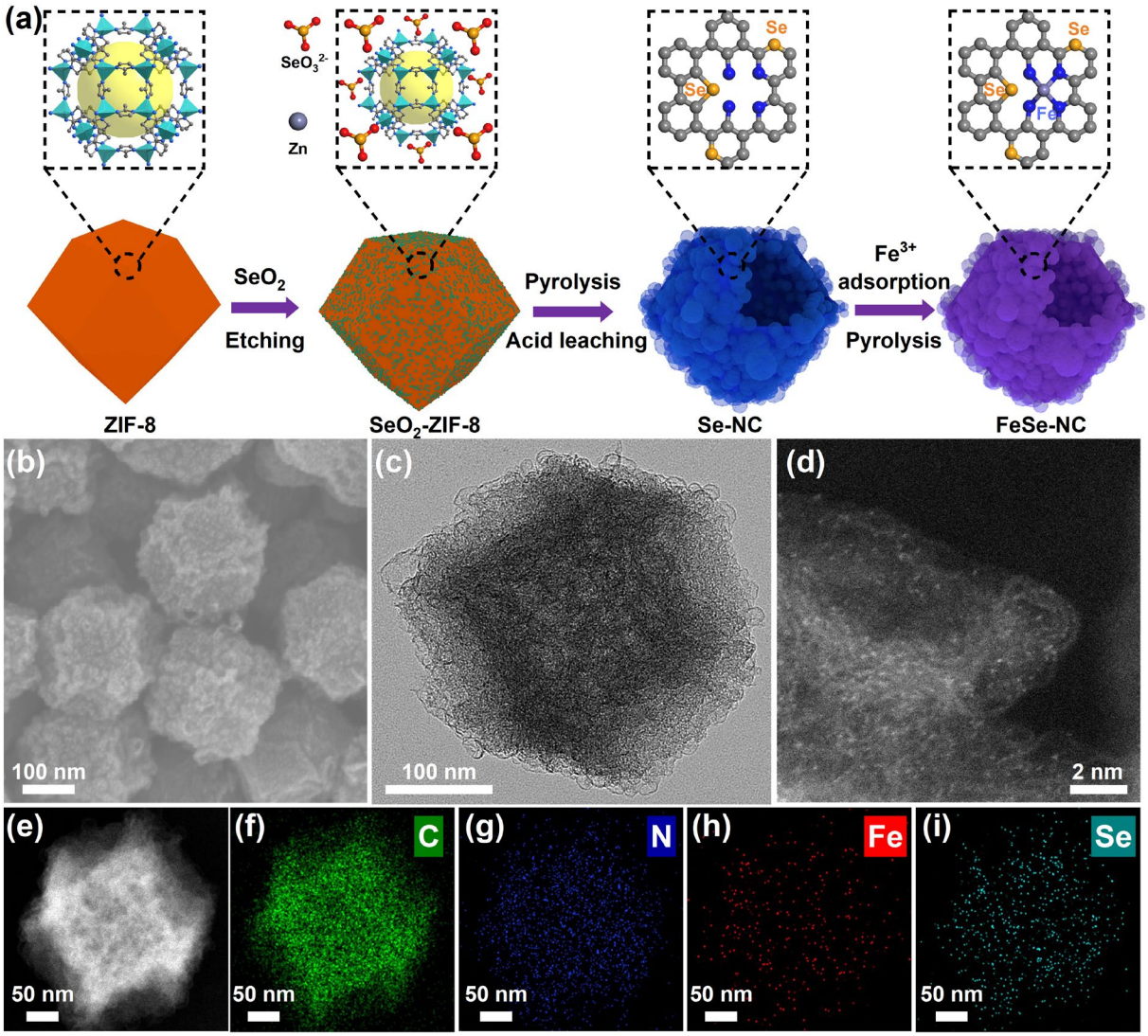

Figure 1. (a) Schematics of the synthetic steps for FeSe-NC. (b) SEM image, (c) TEM image, (d) HAADF-STEM image, and (e–i) EDX mapping results of FeSe-NC.

Figure 1a shows the step-wise synthesis of the hybrid Fe-Se DAC. The well-defined ZIF-8 nanocrystals were first etched by SeO_2 (denoted as SeO_2-ZIF-8), followed by calcination. During

the pyrolysis, the evaporated Se species were reduced and doped into the NC substrate, forming an atomically dispersed Se catalyst (Se-NC) with hierarchical hollow nanostructure. The resulting Se-NC was then utilized as a host to absorb and anchor Fe ions, and a subsequent thermal activation was performed to obtain highly dispersed dual-atom Fe-Se DAC (FeSe-NC). Similarly, the single-atom Fe catalyst (Fe-NC) without SeO_2 etching was prepared for comparative studies.

The structure and morphology of the resultant etching product were first investigated using powder X-ray diffraction (PXRD) and scanning electron microscopy (SEM). Figure S1 shows the PXRD pattern of SeO_2-ZIF-8, which reveals a phase similar to ZIF-8. Besides, the absence of SeO_2 characteristic peaks indicates that the resultant Zn-Se-O species is amorphous. SEM images (Figure S2, Supporting Information) show that SeO_2-ZIF-8 maintains the initial rhombic dodecahedron shape, but the surface becomes much rougher and porous compared with the ZIF-8 crystals. X-ray spectroscopy (EDX) analysis (Figure S3, Supporting Information) confirms the presence of a small amount of Se introduced during the etching of ZIF-8 by SeO_2.

The morphology of the as-obtained DAC and SAC can be evidenced by the SEM and transmission electron microscopy (TEM) images. The samples inherit the original shapes of ZIF-8 crystals with some shrinkage. However, in comparison with Fe-NC dodecahedron (Figure S4, Supporting Information), FeSe-NC (Figures 1b-c) and Se-NC particles (Figure S5, Supporting Information) become hollow with rough surface due to SeO_2 etching. Simultaneously, many bubble-like cavities can be observed on the surface of Se-containing samples, due to the interconnected few-layer graphene (Figure S6c-d, Supporting Information). Such a hierarchical porous nature can improve the accessibility to active centers, thus facilitating mass transfer during the CO_2RR process. Figure 1c shows the HRTEM images, where Fe and Se nanoparticles and nanoclusters are invisible. In addition, only two broad diffraction peaks (23° and 43°) appear in

the PXRD patterns (Figure S7, Supporting Information), associated with the (002) and (101) facets of carbon, further ruling out the existence of metal or oxide phases. High-angle annular dark-field scanning TEM (HAADF-STEM) analysis was performed, and the image shows that both Fe and Se atoms are bright spots at the atomic scale, indicating the uniform heterogenization of Fe and Se atoms on the carbon support (Figure 1d). Besides, the darker color in the center of the dodecahedron particle demonstrates its hollow nanostructure (Figure 1e). The corresponding EDX mapping also shows a homogenous dispersion of Se and Fe over the entire FeSe-NC particle (Figure 1f-i). The inductively coupled plasma (ICP) analysis unveils that the metal contents in FeSe-NC are 0.51 (Fe) and 1.89 wt% (Se) (Table S1, Supporting Information), respectively, close to Fe content in Fe-NC (0.48 wt%) and Se content in Se-NC (2.29 wt%). Raman spectra and pore size analysis indicate that SeO_2-etching and subsequent doping of Se into NC creates a defect-rich structure with a high surface area and hierarchical micro-mesopores (Figures S8-9, Supporting Information), which is consistent with the TEM results.

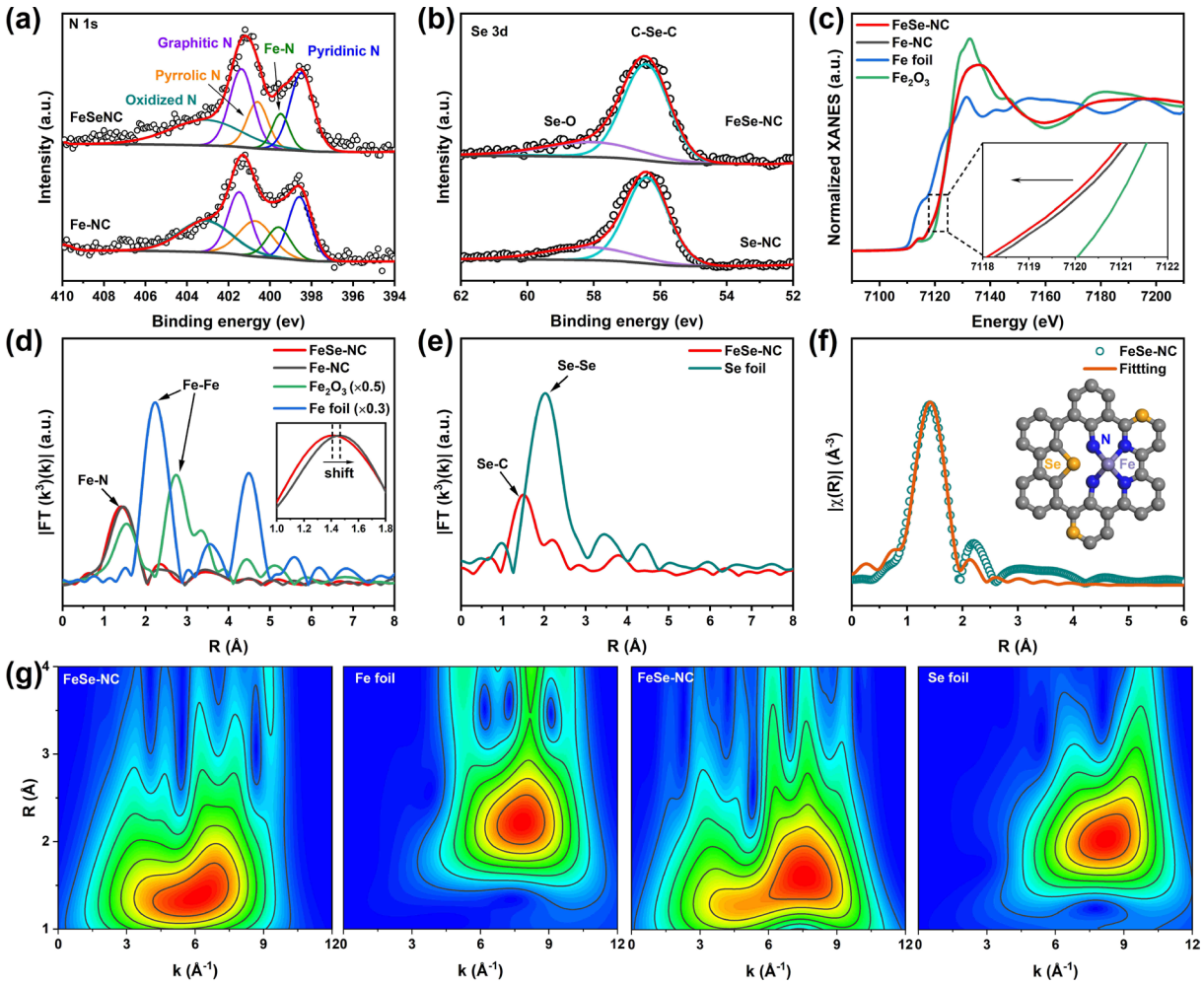

Figure 2. (a) N 1s XPS spectra of Fe-NC and FeSe-NC. (b) Se 3d XPS spectra of FeSe-NC and Se-NC. (c) Normalized Fe K-edge XANES and (d) K-edge EXAFS of FeSe-NC, Fe-NC, Fe_2O_3 and Fe foil. (e) Se K-edge EXAFS of FeSe-NC and Se foil. (f) Fe FT-EXAFS fitting curve of FeSe-NC and the fitting model (inset). (g) Wavelet transform plots of Fe in FeSe-NC and Fe foil; Se in FeSe-NC and Se foil.

X-ray photoelectron spectroscopy (XPS) analysis provides insight into the compositional difference between the catalysts. The survey spectra show that Se only appears in FeSe-NC and Se-NC (Figure S10, Supporting Information). The deconvoluted N 1s profiles suggest that beyond the four typical peaks associated with the pyridinic, pyrrolic, graphitic and oxidized N, an additional peak at 399.5 eV (Fe-N) appears in FeSe-NC and Fe-NC samples, compared to Se-NC

(Figures 2a and S11, Supporting Information).[37] In the high-resolution Se 3d spectra, a central peak for Se-C_2 units (56.4 eV) can be observed,[38, 39] and the peak remains nearly unchanged after high-temperature H_2 etching (Figures 2b and S12, Supporting Information), indicating that the atomically dispersed Se sites have excellent stability. The minor peak belonging to the Se-O bond (58.4 eV) suggests the incomplete reduction of tiny amount of Se species. Regarding the Fe 2p spectra, the binding energy of Fe is higher than metallic Fe, indicating the oxidation state of Fe in FeSe-NC and Fe-NC (Figure S13, Supporting Information).[40] Moreover, the position of Fe $2p_{3/2}$ peak in FeSe-NC experiences a slight red shift by 0.63 eV compared with Fe-NC, suggesting the existence of the electronic interaction between Se and Fe. Similar electronic changes were observed in previous studies.[41]

To study the geometrical coordination of Fe and Se in the as-prepared catalysts, X-ray absorption spectroscopy (XAS) measurement was conducted. The Fe K-edge X-ray absorption near edge structure (XANES) spectra (Figure 2c) demonstrate that the adsorption edges of FeSe-NC and Fe-NC exhibit similar energy between Fe and Fe_2O_3, suggesting that the oxidation state of Fe in both samples is close to +2. The slight difference in the XANES plots may be attributed to the weak electronegativity of the Se atom. However, the absorption edge of FeSe-NC is observed to shift slightly to a lower energy compared with Fe-NC (Figure 2c, inset), implying a higher electron density around the Fe site in FeSe-NC than that in Fe-NC. This indicates the electronic structure around Fe site is influenced by the presence of Se in FeSe-NC, consistent with the XPS analysis which also suggests an electronic interaction between Se and Fe in FeSe-NC. The Fourier transformed extended X-ray absorption fine structure (FT EXAFS, Figure 2d) spectra show similar peaks at ~1.47 Å associated with Fe-N for FeSe-NC and Fe-NC, while the peak at 2.24 Å associated with Fe-Fe is invisible, indicating the atomically dispersed Fe sites.[42, 43] The Se

K-edge XANES spectra suggest that Se in FeSe-NC has a partially positive charge (Figure S14, Supporting Information). Thus, the analytical results from Fe K-edge and Se K-edge XANES spectra reveal charge redistribution between Fe and Se, strongly correlated with the coordination environments. Notably, only Se-C signal (1.50 Å) can be found in the EXAFS spectra (Figure 2e), confirming that the isolated Se atoms are atomically coordinated with C. Quantitative EXAFS fittings indicate that the coordination numbers of the isolated Fe-N and Se-C are 3.7 and 1.9, suggesting that the atomic Fe centers and Se centers feature the geometric Fe-N_4 and Se-C_2 configurations, respectively (Figure 2f and Figures S15-16, Table S2, Supporting Information). In addition, the wavelet transform (WT) plots are in accordance with the above Fourier transform results (Figure 2g).

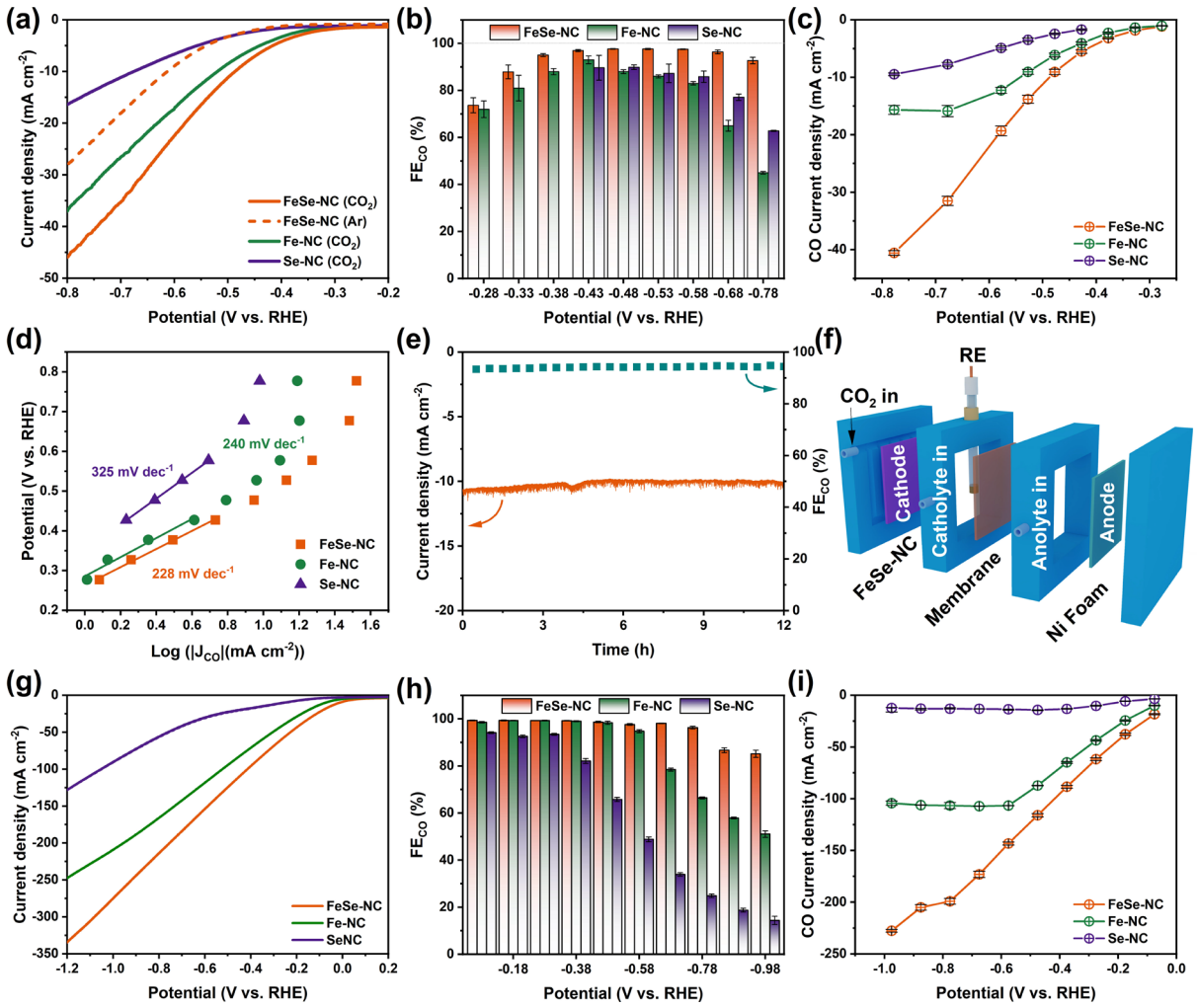

Figure 3. Electrocatalytic CO_2RR performance of the catalysts: (a) LSV curves, (b) FE_{CO}, (c) j_{CO}, (d) Tafel plots, and (e) durability test in the H-type cell. (f) Schematic diagram, (g) LSV curves, (h) FE_{CO}, and (i) j_{CO} in the flow cell.

The electrocatalytic CO_2RR evaluation for these catalysts was first conducted in a conventional H-type cell containing 0.5 M $KHCO_3$ electrolyte. When CO_2RR was assessed by the polarization curves (Figure 3a and Figure S17, Supporting Information), FeSe-NC offered the most positive onset potential and highest j values compared to Fe-NC, Se-NC and NC, showcasing its boosted intrinsic activity. Meanwhile, the superior CO_2RR activity of FeSe-NC is also reflected in the large difference between the current densities recorded in the CO_2 and Ar-saturated electrolytes. We

further performed controlled electrolysis to evaluate the CO_2RR selectivity, during which the gas and liquid products at different applied potentials were detected and quantified via online gas chromatography (GC) and offline nuclear magnetic resonance (NMR) spectroscopy analysis, respectively. In this work, except for H_2 and CO, no other products were detected (Figure S18, Supporting Information). As shown in Figure 3b, the calculated faraday efficiency (FE) results show that FeSe-NC has the best CO_2-to-CO selectivity. Specifically, FeSe-NC exhibits not only the highest FE_{CO} but also the long-last and stable FE_{CO} (>90%) from −0.38 to −0.78 V that surpass those of Fe-NC and Se-NC. Moreover, the maximum FE_{CO} by FeSe-NC reached 97.7% at −0.48 V, while the highest FE_{CO} was only 93% and 90% for Fe-NC and Se-NC, respectively. Combining the total j and FE_{CO}, the derived CO partial current density (j_{CO}) is shown in Figure 3c. Obviously, the j_{CO} of FeSe-NC increased with the applied potentials and reached a maximum of −40.4 mA cm^{-2} at −0.78 V, which significantly outperforms Fe-NC (−15.5 mA cm^{-2}) and Se-NC (−9.5 mA cm^{-2}). Notably, compared with the state-of-the-art Fe-based SACs, FeSe-NC exhibits superior CO_2RR performance in terms of the overpotential, FE_{CO} and j_{CO} (Table S3, Supporting Information). Meanwhile, the calculated turnover frequency (TOF) (Figure S19, Supporting Information), representing the activity of a single site, indicates that Fe-NC (5.6 s^{-1}) has a much higher intrinsic activity for CO_2-to-CO conversion compared to Se-NC (1.2 s^{-1}). Compared to a single Fe and Se site, FeSe-NC affords the highest TOF value of 10.4 s^{-1}, further verifying the synergistic enhancement in the CO_2RR activity upon combining Fe with Se. Additionally, as an important parameter, Tafel slope was acquired to provide kinetic insight into the reaction. The fitting results exhibit the lowest value for FeSe-NC, indicating boosted CO production kinetics after introducing Se SAs (Figure 3d). Such enhanced reaction kinetics are also evidenced by the lower charge-transfer resistance of FeSe-NC and higher double-layer capacitance (C_{dl}) (Figures

S20-21, Supporting Information). Further long-term electrolysis indicates that FeSe-NC also has outstanding durability. After 12 hours of continuous electrolysis, both *j* and FE_{CO} of FeSe-NC maintained the same (Figure 3e). The SEM, TEM, XPS and ICP results show no change in chemical composition and structure after the long-term test, verifying the stability of FeSe-NC (Figures S22-23 and Table S4, Supporting Information).

To further verify the SeO_2-etching effect on the CO_2RR performance, Se-doped Fe-NC catalyst (Fe/Se_p-NC) as a comparison was also fabricated using Se powders under the same conditions. TEM image (Figure S24, Supporting Information) shows that Fe/Se_p-NC appears to be similar to FeSe-NC but without visible bubble-like cavities on the surface. N 1s XPS spectrum shows that the intensity of pyridinic N increased after Se-doping in contrast to FeSe-NC (Figure S25, Supporting Information). Compared with FeSe-NC, the resulting Fe/Se_p-NC catalyst exhibited a lower current density and poor CO selectivity (Figure S26, Supporting Information), likely due to the lack of active sites and the increase of HER-favorable pyridinic N species.[14]

The impact of other factors on performance, such as Se content and etching time, was also studied. Comparative experiments show that neither Se content nor etching time greatly changes the CO_2RR performance of FeSe-NC (Figure S27, Supporting Information) due to their similar Se content after two calcinations. These findings confirm that SeO_2-etching removes some pyridinic N atoms and suppresses the competitive H_2 generation, and also generate active sites that boost the CO_2RR performance.

As discussed above, while FeSe-NC was observed to have high selectivity toward CO in H-type cell, the reaction rates are slow, which is due to the limited mass transfer caused by low CO_2 solubility. Therefore, we further tested the CO_2RR activity of FeSe-NC in a self-designed flow cell electrolyzer (Figure 3f), where high CO_2 transfer rate can be obtained. As shown in Figure 3g,

a significantly higher *j* was achieved in the flow cell due to the enhanced mass transfer, in marked contrast to that gained in the H-type cell. Compared with Fe-NC and Se-NC, FeSe-NC has a significantly higher *j* value (>320 mA cm^{-2}), and its outstanding CO_2RR performance is also verified by its higher FE_{CO} and j_{CO}, as shown in Figures 3h and 3i. The highest j_{CO} of FeSe-NC was realized at −0.98 V, reaching 228 mA cm^{-2} with a high FE_{CO}. The j_{CO} of Fe-NC dropped sharply and struggled to reach 108 mA cm^{-2} as a result of decreased FE_{CO}. Similar degradations were also observed in previously reported Fe-SACs, possibly due to the insufficient CO desorption on Fe centers at high potentials.[44] CO desorption in the local atomic environment, especially at high current density, could become rate limiting and then greatly influence the CO_2RR performance since CO desorption is a non-Faradaic step. Therefore, the incorporation of Se SAs in FeSe-NC promotes CO desorption through electronic structure regulation,[45] which is confirmed by computational and *in situ* analysis (as discussed in later section).

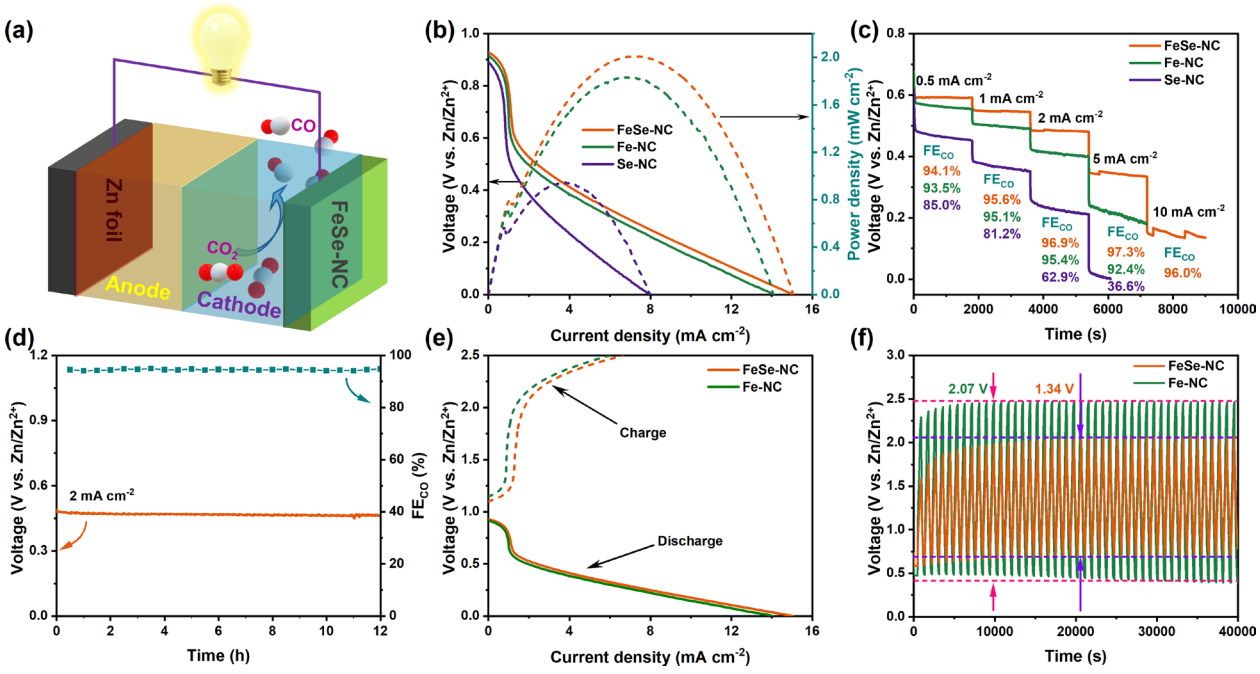

Figure 4. Performance of rechargeable Zn-CO_2 batteries with the FeSe-NC as the cathodes. (a) Schematic representation of aqueous ZCB. (b) Polarization curves with related power densities.

(c) Correlation between discharge plateaus, *j*, and corresponding FE_{CO}. (d) Long-term stability test of ZCB with FeSe-NC at 2 mA cm^{-2}. (e) Discharging-charging polarization curves. (f) Galvanostatic cycling performance at 0.5 mA cm^{-2}.

Inspired by the impressive CO_2RR performance, FeSe-NC was further applied as the cathode material and integrated into an aqueous rechargeable Zn-CO_2 battery (ZCB) (Figure 4a). As shown in Figure 4b, the peak power density of FeSe-NC-based ZCB was achieved at 0.27 V, reaching 2.01 mW cm^{-2} with a current density of 7.43 mA cm^{-2}, surpassing those of Fe-NC (1.83 mW cm^{-2}, 6.68 mA cm^{-2}). In addition, ZCB with FeSe-NC has better rate performance and higher FE_{CO} (>94%) when discharging at various current densities (Figure 4c). The stability of FeSe-NC-based ZCB was then evaluated with a 12 h discharging at 2 mA cm^{-2}, where no obvious decay was observed in either voltage and FE_{CO} (Figure 4d). As for the rechargeable performance, FeSe-NC exhibits a comparatively small charging-discharging gap of only 1.34 V, suggesting its superior reversibility compared to Fe-NC (2.07 V) (Figures 4e and 4f).

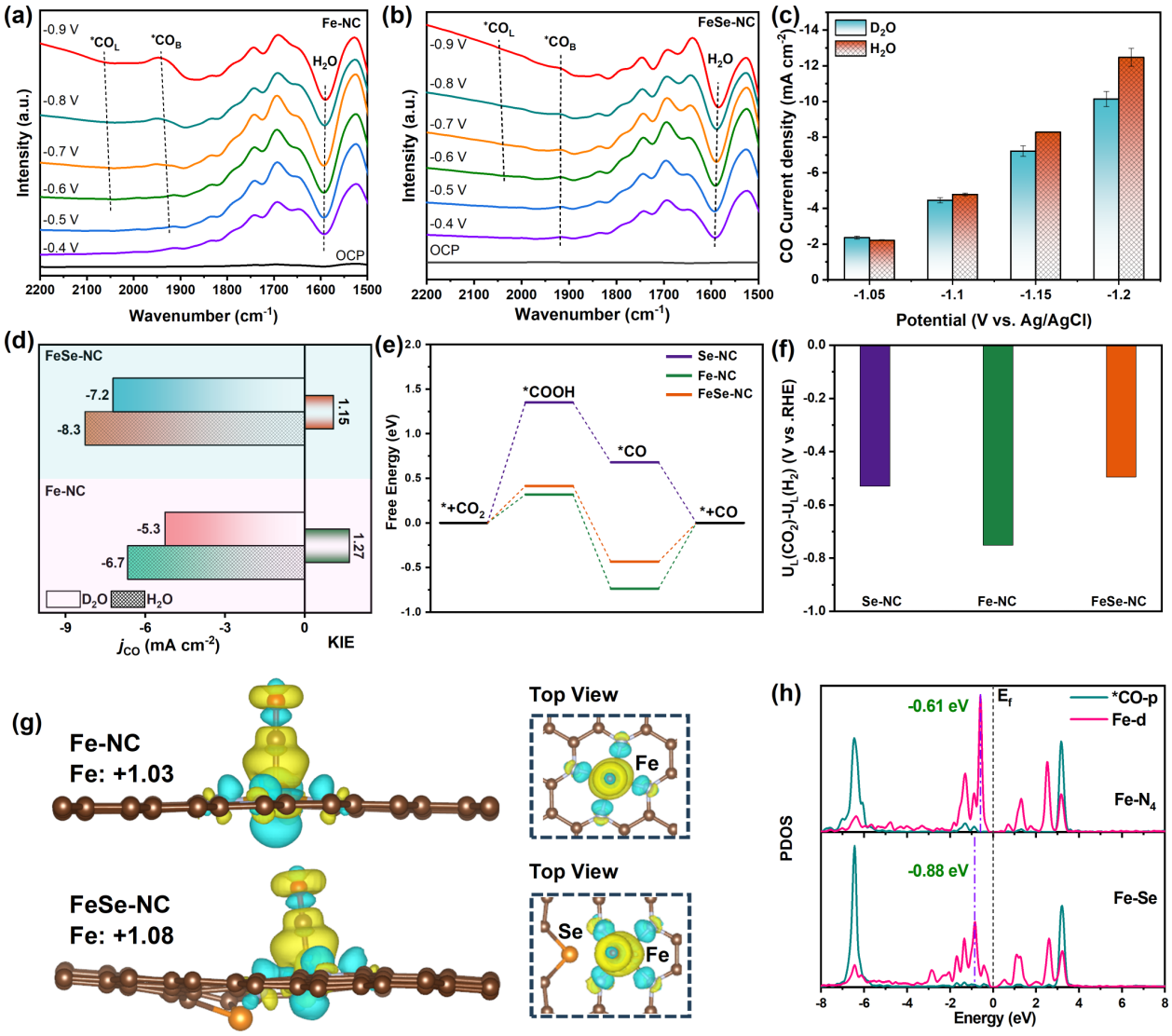

Figure 5. *In situ* ATR-FTIR spectra of (a) Fe-NC and (b) FeSe-NC. (c) The j_{CO} of FeSe-NC in H_2O and D_2O at different potentials. (d) Comparison of the KIE values of FeSe-NC and Fe-NC. Calculations for FeSe-NC, Fe-NC and Se-NC: (e) Gibbs free energy profiles for CO_2RR; (f) differences in limiting potentials for CO_2RR ($U_L(CO_2)$) and HER ($U_L(H_2)$); (g) electron density difference and Bader charge analysis of Fe-NC and FeSe-NC with adsorption of *CO on Fe sites. Electron accumulation and depletion are marked with light yellow and cyan, respectively; (h) PDOS of *d* orbitals of Fe in FeSe-NC and Fe-NC.

To explore the origin of CO_2RR activity enhancement for FeSe-NC, the *in-situ* attenuated total reflection Fourier transform infrared spectroscopy (ATR-FTIR) was performed to study the dynamics of intermediates during the electrochemical process. As displayed in Figure 5a, two *CO absorption peaks around 1930 and 2060 cm^{-1} were observed for Fe-NC, indicating the presence of a strong bridge-bonded (*CO_B) and very weak linear-bonded *CO (*CO_L) species, respectively.[46-48] Moreover, the increased frequencies and intensity of the *CO_B bands at the potentials negative than −0.7 V (for Fe-NC) suggest a higher CO coverages.[49] In sharp contrast, these peaks were much weaker for FeSe-NC, indicating that *CO desorption occurs more easily on FeSe-NC (Figure 5b), which is consistent with the electrochemical results that the overall performance for CO production is significantly enhanced. Furthermore, a comparative kinetic isotope effect (KIE) analysis revealed a facilitated proton transfer for FeSe-NC after introducing Se, as evidenced by its smaller KIE value (Figure 5c-d and Figure S28, Supporting Information).[50]

Density functional theory (DFT) calculations were executed to explore the contribution of Se SAs in modulating the electrocatalytic CO_2RR process in FeSe-NC. Based on the XAS results, the FeN_4 configuration with SeC_2 edge in FeSe-NC was used for theoretical analysis. Meanwhile, the comparative Fe-N_4 and Se-C_2 models were also built for Fe-NC and Se-NC, respectively. As displayed in Figure 5e, the calculated Gibbs free energy diagrams for the pathways suggest that activating CO_2 to intermediate *COOH on Se-NC is an endothermic process with an uphill energy change. The large energy barrier, therefore, results in a higher onset potential of Se-NC during CO_2RR measurements. By contrast, both Fe SAC samples offer a considerable decrease in the energy barriers for *COOH formation, which suggests that CO_2RR is more favorable to take place on Fe sites, evidenced by their smaller initial potentials. Moreover, introducing Se atoms can decrease the *CO binding strength and promote the desorption of CO on neighbouring FeN_4 sites,

thus facilitating the catalytic performance, consistent with electrochemical and ATR-FTIR results. The difference between the thermodynamic limiting potentials for CO production and competitive H_2 evolution (denoted as $U_L(CO_2)$-$U_L(H_2)$, (U_L=-ΔG_0/e)) is important in evaluating the selectivity of the catalysts. As depicted in Figure 5f, the difference value of FeSe-NC is much more positive than that of Fe-NC, indicating that the CO selectivity of Fe-N_4 can be improved by adjacent Se dopants, resulting in a higher FE_{CO}.

The charge density distribution analysis was also performed to depict the charge accumulation or depletion at the atomic Fe and Fe-Se sites. The corresponding results indicate an obvious interaction between Fe and Se atoms leading to an asymmetric electronic structure (Figure 5g, Figure S29 and Table S5, Supporting Information), which aligns well with the XPS and XANES analyses. Furthermore, the projected density of states (PDOS) provides insights into the energy state of Fe atoms in Fe SA and Fe-Se DA (Figure 5h). After introducing adjacent Se atoms, the *d*-band center of Fe shifts negatively from −0.61 to −0.88 eV due to the strong Fe-Se interactions, which is favorable for *CO desorption during the CO_2RR process, thus exhibiting superior CO selectivity. Therefore, the theoretical analyses reveal that the asymmetric electronic properties induced by Se SA not only offer more active and selective effect but also inhibit the competitive HER reaction, thus boosting the overall CO_2RR electrocatalytic performance, which matches well with the electrochemical observations.

CONCLUSION

In conclusion, we have developed a facile selenic acid etching-assisted strategy to fabricate metal-semimetal Fe-Se dual single-atom sites in a MOF-derived porous hollow NC matrix. Benefitting from the synergetic FeN_4 and SeC_2 atomic configurations, FeSe-NC delivers

exceptional CO_2RR activity for selective CO generation, featuring a high FE_{CO} (>97%) and industrial-level j_{CO} (228 mA cm^{-2}), surpassing the majority of prevailing Fe-based catalysts. Experiments and DFT calculations illustrate that the electronic configuration of Fe-Se hybrid sites facilitates CO_2 activation and optimizes the binding strength of the key intermediates on active sites, thus boosting CO_2 conversion. Besides, SeO_2 etching also enhances the overall CO_2RR by increasing surface roughness, porosity and active site accessibility. This etching-doping atomic engineering provides a straightforward approach to fabricating hybrid dual-metal single-atom catalysts for CO_2RR and other chemical reactions.

METHODS

Synthesis of SeO_2-ZIF-8. ZIF-8 was first synthesized following a literature method.[51] Then, 400 mg of ZIF-8 was dispersed in 20 mL of MeOH, upon which 20 mL of aqueous solution containing 50 mg of SeO_2 was added and aged for 30 min. After that, SeO_2-ZIF-8 was collected by centrifugation, washed with methanol, and dried overnight at 60 °C under vacuum.

Synthesis of Se-NC. In a typical synthesis, SeO_2-ZIF-8 was transferred to a quartz tube and pyrolyzed at 1000 °C for 2 h with a ramping rate of 5 °C min^{-1} under Ar flow, and the sample was cooled down to room temperature naturally. For comparison, NCs were also synthesized by a similar method in the absence of SeO_2.

Synthesis of FeSe-NC and Fe-NC. The as-prepared Se-NC was immersed in a HCl solution (2.0 M) and stirred at 80 °C for 12 h to remove Zn species. The FeSe-NC catalyst was prepared via metal ion adsorption using the Se-NC as a porous carbon host followed by thermal activation. For example, 50 mg of Se-NC powders were dispersed in 5 mL of isopropanol that contained 2.5 mg of $Fe(NO_3)_3 \cdot 9H_2O$. The as-obtained mixture was then sonicated for 1.0 h and stirred 2.0 h before

being washed with methanol, centrifuged, and dried at 60 °C overnight to prepare the Se-NC-Fe^{3+} sample. Afterward, the obtained Se-NC-Fe^{3+} was subjected to heat treatment at 900 °C with a ramp rate of 10 °C min^{-1} for 1.0 h under Ar and cooled naturally to generate the final FeSe-NC catalyst. As another control, Fe-NC was obtained following the same procedure except that NC was used as the carbon host.

Synthesis of Fe/Se_p-NC. The synthesis process for is similar to that of FeSe-NC, except that SeO_2 was replaced by Se powders.

Electrochemical measurement

H-type cell system. Electrochemical CO_2RR measurements were conducted in a gas-tight H-type cell, in which the anodic and cathodic chambers were separated by a proton exchange membrane (Nafion 117). Ag/AgCl (in saturated KCl aqueous) electrode and Pt mesh were used as the reference and counter electrodes, respectively. Before each experiment, CO_2 (99.999%) was constantly purged into the catholyte (30 mL) for 30 minutes to form a CO_2-saturated electrolyte. LSV curves were recorded in Ar or CO_2-saturated 0.5 M $KHCO_3$ electrolyte with a scan rate of 10 mV s^{-1}. All potentials reported here were converted to the RHE scale.

Flow cell system. Electrochemical experiments were performed in a flow cell reactor filled with gas, catholyte, and anolyte. The catalyst-supported gas diffusion electrode (GDE) with a mass loading of 1 mg cm^{-2}, Ag/AgCl (in saturated KCl aqueous) electrode, and nickel foam were used as the cathode, reference electrode, and anode, respectively. Copper tapes were used to connect the cathode and anode. The anolyte and catholyte chambers were separated by an anionic exchange membrane (Fumasep FAB-PK-130). 80 mL of electrolyte (1 M KOH, pH ≈14.0) was circulated in the cathode and anode chamber using a peristaltic pump at a constant flow of 30 mL min^{-1}. High-

purity CO_2 was directly fed to the backside of the cathode GDE at a constant flow of 40.0 sccm using a digital mass flow controller, and CO_2 output was connected to a GC system.

ASSOCIATED CONTENT

Supporting Information.

The Supporting Information is available free of charge.

Characterizations, additional SEM images, TEM images, elemental analysis, XRD patterns, N_2 adsorption−desorption results, ICP-OES results, more electrocatalytic tests (PDF)

AUTHOR INFORMATION

Corresponding Authors

Qi-Long Zhu - *State Key Laboratory of Structural Chemistry, Fujian Institute of Research on the Structure of Matter, Chinese Academy of Sciences (CAS), Fuzhou 350002, China; School of Materials Science and Engineering, Zhejiang Sci-Tech University, Hangzhou 310018, China*

E-mail: qlzhu@fjirsm.ac.cn

Zhenguo Huang - *School of Civil and Environmental Engineering, University of Technology Sydney, Ultimo, New South Wales 2007, Australia*

E-mail: zhenguo.huang@uts.edu.au

Author Contributions

The manuscript was written through contributions of all authors. All authors have given approval to the final version of the manuscript.

Notes

The authors declare no competing financial interest.

ACKNOWLEDGMENTS

Q. Zhu acknowledges the support under the National Key Research and Development Program of China (2021YFA1500402), the National Natural Science Foundation of China (NSFC) (22175174 and 52332007), the Natural Science Foundation of Fujian Province (2022L3092). Z. Huang acknowledges Australian Research Council's Discovery Projects funding scheme (DP220103458) and Future Fellowship (FT190100658).

REFERENCES

(1) Ross, M. B.; De Luna, P.; Li, Y.; Dinh, C.-T.; Kim, D.; Yang, P.; Sargent, E. H. Designing materials for electrochemical carbon dioxide recycling. *Nature Catalysis* **2019**, *2* (8), 648-658.

(2) Wang, G.; Chen, J.; Ding, Y.; Cai, P.; Yi, L.; Li, Y.; Tu, C.; Hou, Y.; Wen, Z.; Dai, L. Electrocatalysis for CO_2 conversion: from fundamentals to value-added products. *Chem.Soc.Rev.* **2021**, *50* (8), 4993-5061.

(3) Jin, S.; Hao, Z.; Zhang, K.; Yan, Z.; Chen, J. Advances and Challenges for the Electrochemical Reduction of CO_2 to CO: From Fundamentals to Industrialization. *Angew. Chem. Int. Ed.* **2021**, *60* (38), 20627-20648.

(4) Zhu, D. D.; Liu, J. L.; Qiao, S. Z. Recent Advances in Inorganic Heterogeneous Electrocatalysts for Reduction of Carbon Dioxide. *Adv. Mater.* **2016**, *28* (18), 3423-3452.

(5) Costentin, C.; Robert, M.; Savéant, J.-M. Catalysis of the electrochemical reduction of carbon dioxide. *Chem.Soc.Rev.* **2013**, *42* (6), 2423-2436.

(6) Wang, Y.; Su, H.; He, Y.; Li, L.; Zhu, S.; Shen, H.; Xie, P.; Fu, X.; Zhou, G.; Feng, C.; et al. Advanced Electrocatalysts with Single-Metal-Atom Active Sites. *Chem. Rev.* **2020**, *120* (21), 12217-12314.

(7) Han, S.-G.; Ma, D.-D.; Zhu, Q.-L. Atomically Structural Regulations of Carbon-Based Single-Atom Catalysts for Electrochemical CO_2 Reduction. *Small Methods* **2021**, *5* (8), 2100102.

(8) Wang, Y.; Liu, Y.; Liu, W.; Wu, J.; Li, Q.; Feng, Q.; Chen, Z.; Xiong, X.; Wang, D.; Lei, Y. Regulating the coordination structure of metal single atoms for efficient electrocatalytic CO_2 reduction. *Energy Environ. Sci.* **2020**, *13* (12), 4609-4624.

(9) Zhou, S.-H.; Wei, W.; Cai, X.; Ma, D.-D.; Wang, S.-M.; Li, X.; Zhu, Q.-L. Customizing Highly Asymmetrical Coordination Microenvironment into P-Block Metal Single-Atom Sites to Boost Electrocatalytic CO_2 Reduction. *Adv. Funct. Mater.* **2023**, *34* (6), 2311422.

(10) Zhang, Z.; Zhu, J.; Chen, S.; Sun, W.; Wang, D. Liquid Fluxional Ga Single Atom Catalysts for Efficient Electrochemical CO_2 Reduction. *Angew. Chem. Int. Ed.* **2023**, *62* (3), e202215136.

(11) Gan, T.; Wang, D. Atomically dispersed materials: Ideal catalysts in atomic era. *Nano Res.* **2024**, *17* (1), 18-38.

(12) Ye, Y.; Cai, F.; Li, H.; Wu, H.; Wang, G.; Li, Y.; Miao, S.; Xie, S.; Si, R.; Wang, J. J. N. E. Surface functionalization of ZIF-8 with ammonium ferric citrate toward high exposure of Fe-N active sites for efficient oxygen and carbon dioxide electroreduction. *Nano Energy* **2017**, *38*, 281-289.

(13) Cao, C.; Zhou, S.; Zuo, S.; Zhang, H.; Chen, B.; Huang, J.; Wu, X.-T.; Xu, Q.; Zhu, Q.-L. Si Doping-Induced Electronic Structure Regulation of Single-Atom Fe Sites for Boosted CO_2 Electroreduction at Low Overpotentials. *Research* **2023**, *6*, 0079.

(14) Liu, C.; Wu, Y.; Sun, K.; Fang, J.; Huang, A.; Pan, Y.; Cheong, W.-C.; Zhuang, Z.; Zhuang, Z.; Yuan, Q. Constructing FeN_4/graphitic nitrogen atomic interface for high-efficiency electrochemical CO_2 reduction over a broad potential window. *Chem* **2021**, *7* (5), 1297-1307.

(15) Zhang, Z.; Xiao, J.; Chen, X.-J.; Yu, S.; Yu, L.; Si, R.; Wang, Y.; Wang, S.; Meng, X.; Wang, Y.; et al. Reaction Mechanisms of Well-Defined Metal–N_4 Sites in Electrocatalytic CO_2 Reduction. *Angew. Chem. Int. Ed.* **2018**, *57* (50), 16339-16342.

(16) Sun, X.; Tuo, Y.; Ye, C.; Chen, C.; Lu, Q.; Li, G.; Jiang, P.; Chen, S.; Zhu, P.; Ma, M.; et al. Phosphorus Induced Electron Localization of Single Iron Sites for Boosted CO_2 Electroreduction Reaction. *Angew. Chem. Int. Ed.* **2021**, *60* (44), 23614-23618.

(17) Gao, Y.; Liu, B.; Wang, D. J. A. M. Microenvironment Engineering of Single/Dual‐atom Catalysts for Electrocatalytic Application. *Adv. Mater.* **2023**, 2209654.
(18) Li, R.; Wang, D. Superiority of Dual-Atom Catalysts in Electrocatalysis: One Step Further Than Single-Atom Catalysts. *Adv. Energy Mater.* **2022**, *12* (9), 2103564.
(19) Zhang, W.; Chao, Y.; Zhang, W.; Zhou, J.; Lv, F.; Wang, K.; Lin, F.; Luo, H.; Li, J.; Tong, M.; et al. Emerging Dual-Atomic-Site Catalysts for Efficient Energy Catalysis. *Adv. Mater.* **2021**, *33* (36), 2102576.
(20) Li, Y.; Wang, H.; Yang, X.; O'Carroll, T.; Wu, G. Designing and Engineering Atomically Dispersed Metal Catalysts for CO_2 to CO Conversion: From Single to Dual Metal Sites. *Angew. Chem. Int. Ed.* **2023**, *63* (12), e202317884.
(21) Xie, W.; Li, H.; Cui, G.; Li, J.; Song, Y.; Li, S.; Zhang, X.; Lee, J. Y.; Shao, M.; Wei, M. NiSn Atomic Pair on an Integrated Electrode for Synergistic Electrocatalytic CO_2 Reduction. *Angew. Chem. Int. Ed.* **2021**, *60* (13), 7382-7388.
(22) Fan, Z.; Luo, R.; Zhang, Y.; Zhang, B.; Zhai, P.; Zhang, Y.; Wang, C.; Gao, J.; Zhou, W.; Sun, L.; et al. Oxygen-Bridged Indium-Nickel Atomic Pair as Dual-Metal Active Sites Enabling Synergistic Electrocatalytic CO_2 Reduction. *Angew. Chem. Int. Ed.* **2023**, *62* (7), e202216326.
(23) Li, Y.; Shan, W.; Zachman, M. J.; Wang, M.; Hwang, S.; Tabassum, H.; Yang, J.; Yang, X.; Karakalos, S.; Feng, Z.; et al. Atomically Dispersed Dual-Metal Site Catalysts for Enhanced CO_2 Reduction: Mechanistic Insight into Active Site Structures. *Angew. Chem. Int. Ed.* **2022**, *61* (28), e202205632.
(24) Li, Y.; Wei, B.; Zhu, M.; Chen, J.; Jiang, Q.; Yang, B.; Hou, Y.; Lei, L.; Li, Z.; Zhang, R.; et al. Synergistic Effect of Atomically Dispersed Ni–Zn Pair Sites for Enhanced CO_2 Electroreduction. *Adv. Mater.* **2021**, *33* (41), 2102212.
(25) Ren, W.; Tan, X.; Yang, W.; Jia, C.; Xu, S.; Wang, K.; Smith, S. C.; Zhao, C. Isolated Diatomic Ni-Fe Metal–Nitrogen Sites for Synergistic Electroreduction of CO_2. *Angew. Chem. Int. Ed.* **2019**, *58* (21), 6972-6976.
(26) Pei, J.; Wang, T.; Sui, R.; Zhang, X.; Zhou, D.; Qin, F.; Zhao, X.; Liu, Q.; Yan, W.; Dong, J. N-Bridged Co–N–Ni: new bimetallic sites for promoting electrochemical CO_2 reduction. *Energy Environ. Sci.* **2021**, *14* (5), 3019-3028.

(27) Yan, C.; Li, H.; Ye, Y.; Wu, H.; Cai, F.; Si, R.; Xiao, J.; Miao, S.; Xie, S.; Yang, F.; et al. Coordinatively unsaturated nickel–nitrogen sites towards selective and high-rate CO_2 electroreduction. *Energy Environ. Sci.* **2018**, *11* (5), 1204-1210.

(28) Zhao, C.; Dai, X.; Yao, T.; Chen, W.; Wang, X.; Wang, J.; Yang, J.; Wei, S.; Wu, Y.; Li, Y. Ionic Exchange of Metal–Organic Frameworks to Access Single Nickel Sites for Efficient Electroreduction of CO_2. *J. Am. Chem. Soc.* **2017**, *139* (24), 8078-8081.

(29) Wang, X.; Fu, N.; Liu, J.-C.; Yu, K.; Li, Z.; Xu, Z.; Liang, X.; Zhu, P.; Ye, C.; Zhou, A.; et al. Atomic Replacement of PtNi Nanoalloys within Zn-ZIF-8 for the Fabrication of a Multisite CO_2 Reduction Electrocatalyst. *J. Am. Chem. Soc.* **2022**, *144* (50), 23223-23229.

(30) Shang, H.; Wang, T.; Pei, J.; Jiang, Z.; Zhou, D.; Wang, Y.; Li, H.; Dong, J.; Zhuang, Z.; Chen, W.; et al. Design of a Single-Atom Indium$^{\delta+}$–N_4 Interface for Efficient Electroreduction of CO_2 to Formate. *Angew. Chem. Int. Ed.* **2020**, *59* (50), 22465-22469.

(31) Cai, Z. X.; Wang, Z. L.; Xia, Y. J.; Lim, H.; Zhou, W.; Taniguchi, A.; Ohtani, M.; Kobiro, K.; Fujita, T.; Yamauchi, Y. Tailored Catalytic Nanoframes from Metal–Organic Frameworks by Anisotropic Surface Modification and Etching for the Hydrogen Evolution Reaction. *Angew. Chem. Int. Ed.* **2021**, *60* (9), 4747-4755.

(32) Feng, Y.; Yao, J. Tailoring the structure and function of metal organic framework by chemical etching for diverse applications. *Coord. Chem. Rev.* **2022**, *470*, 214699.

(33) Zhang, L.; Lu, C.; Ye, F.; Pang, R.; Liu, Y.; Wu, Z.; Shao, Z.; Sun, Z.; Hu, L. Selenic Acid Etching Assisted Vacancy Engineering for Designing Highly Active Electrocatalysts toward the Oxygen Evolution Reaction. *Adv. Mater.* **2021**, *33* (14).

(34) Jiang, Y.; Song, Y.; Pan, Z.; Meng, Y.; Jiang, L.; Wu, Z.; Yang, P.; Gu, Q.; Sun, D.; Hu, L. Rapid Amorphization in Metastable $CoSeO_3 \cdot H_2O$ Nanosheets for Ultrafast Lithiation Kinetics. *ACS Nano* **2018**, *12* (5), 5011-5020.

(35) Zhang, B.; Zhang, J.; Zhang, F.; Zheng, L.; Mo, G.; Han, B.; Yang, G. Selenium‐Doped Hierarchically Porous Carbon Nanosheets as an Efficient Metal‐Free Electrocatalyst for CO_2 Reduction. *Adv. Funct. Mater.* **2019**, *30* (3).

(36) Hu, H.; Wang, J.; Cui, B.; Zheng, X.; Lin, J.; Deng, Y.; Han, X. Atomically Dispersed Selenium Sites on Nitrogen-Doped Carbon for Efficient Electrocatalytic Oxygen Reduction. *Angew. Chem. Int. Ed.* **2022**, *61* (3), e202114441.

(37) Chen, Y.; Ji, S.; Wang, Y.; Dong, J.; Chen, W.; Li, Z.; Shen, R.; Zheng, L.; Zhuang, Z.; Wang, D.; et al. Isolated Single Iron Atoms Anchored on N‐Doped Porous Carbon as an Efficient Electrocatalyst for the Oxygen Reduction Reaction. *Angew. Chem. Int. Ed.* **2017**, *56* (24), 6937-6941.

(38) Wang, T.; Wang, Q.; Wang, Y.; Da, Y.; Zhou, W.; Shao, Y.; Li, D.; Zhan, S.; Yuan, J.; Wang, H. Atomically dispersed semimetallic selenium on porous carbon membrane as an electrode for hydrazine fuel cells. *Angew. Chem. Int. Ed.* **2019**, *58* (38), 13466-13471.

(39) Li, F.; Li, T.; Sun, C.; Xia, J.; Jiao, Y.; Xu, H. Selenium-Doped Carbon Quantum Dots for Free-Radical Scavenging. *Angew. Chem. Int. Ed.* **2017**, *56* (33), 9910-9914.

(40) Chen, X.; Ma, D.-D.; Chen, B.; Zhang, K.; Zou, R.; Wu, X.-T.; Zhu, Q.-L. Metal–organic framework-derived mesoporous carbon nanoframes embedded with atomically dispersed Fe–Nx active sites for efficient bifunctional oxygen and carbon dioxide electroreduction. *Appl. Catal B-Environ.* **2020**, *267*, 118720.

(41) Qin, J.; Liu, H.; Zou, P.; Zhang, R.; Wang, C.; Xin, H. L. J. J. o. t. A. C. S. Altering ligand fields in single-atom sites through second-shell anion modulation boosts the oxygen reduction reaction. *J. Am. Chem. Soc.* **2022**, *144* (5), 2197-2207.

(42) Chen, J.; Li, H.; Fan, C.; Meng, Q.; Tang, Y.; Qiu, X.; Fu, G.; Ma, T. Dual Single-Atomic Ni-N_4 and Fe-N_4 Sites Constructing Janus Hollow Graphene for Selective Oxygen Electrocatalysis. *Adv. Mater.* **2020**, *32* (30), 2003134.

(43) Hou, C.-C.; Zou, L.; Sun, L.; Zhang, K.; Liu, Z.; Li, Y.; Li, C.; Zou, R.; Yu, J.; Xu, Q. Single-Atom Iron Catalysts on Overhang-Eave Carbon Cages for High-Performance Oxygen Reduction Reaction. *Angew. Chem. Int. Ed.* **2020**, *59* (19), 7384-7389.

(44) Gu, J.; Hsu, C.-S.; Bai, L.; Chen, H. M.; Hu, X. Atomically dispersed Fe^{3+} sites catalyze efficient CO_2 electroreduction to CO. *Science* **2019**, *364* (6445), 1091-1094.

(45) Sun, K.; Yu, K.; Fang, J.; Zhuang, Z.; Tan, X.; Wu, Y.; Zeng, L.; Zhuang, Z.; Pan, Y.; Chen, C. Nature-Inspired Design of Molybdenum-Selenium Dual-Single-Atom Electrocatalysts for CO_2 Reduction. *Adv. Mater.* **2022**, *34* (44), e2206478.

(46) Zhu, S.; Li, T.; Cai, W.-B.; Shao, M. CO_2 Electrochemical Reduction As Probed through Infrared Spectroscopy. *ACS Energy Lett.* **2019**, *4* (3), 682-689.

(47) Jiang, T.-W.; Zhou, Y.-W.; Ma, X.-Y.; Qin, X.; Li, H.; Ding, C.; Jiang, B.; Jiang, K.; Cai, W.-B. Spectrometric Study of Electrochemical CO_2 Reduction on Pd and Pd-B Electrodes. *ACS Catal.* **2021**, *11* (2), 840-848.

(48) Bao, Y.; Xiao, J.; Huang, Y.; Li, Y.; Yao, S.; Qiu, M.; Yang, X.; Lei, L.; Li, Z.; Hou, Y.; et al. Regulating Spin Polarization via Axial Nitrogen Traction at Fe-N_5 Sites Enhanced Electrocatalytic CO_2 Reduction for Zn-CO_2 Batteries. *Angew. Chem. Int. Ed.* **2024**, *n/a* (n/a), e202406030.

(49) Hammaker, R. M.; Francis, S. A.; Eischens, R. P. Infrared study of intermolecular interactions for carbon monoxide chemisorbed on platinum. *Spectrochimica Acta* **1965**, *21* (7), 1295-1309.

(50) Chen, S.; Li, X.; Kao, C.-W.; Luo, T.; Chen, K.; Fu, J.; Ma, C.; Li, H.; Li, M.; Chan, T.-S.; et al. Unveiling the Proton-Feeding Effect in Sulfur-Doped Fe−N−C Single-Atom Catalyst for Enhanced CO_2 Electroreduction. *Angew. Chem. Int. Ed.* **2022**, *61* (32), e202206233.

(51) Avci, C.; Ariñez‐Soriano, J.; Carné‐Sánchez, A.; Guillerm, V.; Carbonell, C.; Imaz, I.; Maspoch, D. Post‐Synthetic Anisotropic Wet‐Chemical Etching of Colloidal Sodalite ZIF Crystals. *Angew. Chem. Int. Ed.* **2015**, *54* (48), 14417-14421.